Research Article | Vol. 28, No. 23 / 9 November 2020 / Optics Express 35108
Optics EXPRESS

Broadband single-channel coherent perfect absorption with a perfect magnetic mirror

YEONGHOON JIN AND KYOUNGSIK YU*

School of Electrical Engineering, Korea Advanced Institute of Science and Technology (KAIST), 291 Daehak-Ro, Yuseong-Gu, Daejeon 34141, Republic of Korea
ksyu@kaist.edu

Abstract: Two-channel coherent perfect absorption (CPA) enables absorption modulation as well as perfect absorption in a very simple way. However, because of its narrow and discrete operable wavelength range, the CPA has been limited to specific applications. In this work, we theoretically and experimentally demonstrate broadband *single-channel* CPA operable from the visible to near-infrared wavelengths, using an ultrathin absorbing material on a pseudo perfect magnetic mirror. Our simple yet effective method can be applied to various applications such as solar cells, thermophotovoltaics, and stealth technology.

1. Introduction

Optical absorption, reflection and transmission properties play critical roles in a number of applications, such as solar energy harvesting, photodetection, beam steering, and optical modulation [1–9]. Various optical techniques have been reported to surpass conventional limits for such applications, and examples include high-index resonators [3], metamaterials and metasurfaces [4–6], epsilon-near-zero materials [7–9], and coherent perfect absorption (CPA) [10–14]. CPA in particular has attracted great attention because it enables efficient absorption modulation as well as complete light absorption, and does not require complex fabrication processes for such essential operations.

CPA involves two counter-propagating coherent monochromatic waves with the same intensity that are simultaneously incident on the front and back side of an optically absorbing material. The output intensity varies depending on the relative phase difference between two coherent waves [11,12]. Absorption modulation results from the interplay of the absorption and interference of the two waves. *Two-channel* (or double-sided) CPA with two separate external illumination sources has been experimentally demonstrated, using a silicon wafer as an absorbing material [11]. Unfortunately, CPA is known to occur only under specific phase relationships between the two counter-propagating incident waves, and therefore only a discrete set of input wavelengths satisfies such conditions, resulting in discrete and narrowband operations. Accordingly, the two-channel CPA had been considered inappropriate for broadband applications, such as solar energy harvesting and anti-reflecting stealth technologies. However, it was later revealed that broadband two-channel CPA can be realized when the absorbing film is very thin compared to the operation wavelength [15].

On the other hand, it is well known that *single-channel* CPA can be achieved with a combination of a thin absorbing film, lossless dielectric layer, and perfect electric mirror (PEM), and such a structure is known as an asymmetric Fabry-Pérot cavity and Salisbury screen. By controlling the interference between the input wave and the reflected wave through the optical thickness of the dielectric spacer layer between the absorbing film and the PEM surface, the overall absorption at the absorbing film can be significantly increased. Although such a single-channel geometry with a perfect mirror has been reported before, it only works at a narrow wavelength range, not over a broad wavelength range [16,17]. Another previous study demonstrated broadband single-channel CPA in the gigahertz frequency region using a high-impedance reflective surface and ultrathin

#408494 https://doi.org/10.1364/OE.408494
Journal © 2020 Received 16 Sep 2020; revised 22 Oct 2020; accepted 22 Oct 2020; published 4 Nov 2020

Optics EXPRESS

conducting (absorbing) film [18]. A high-impedance surface corresponds to a perfect magnetic mirror (PMM), which blocks and reflects an incident magnetic field, and results in an electric field anti-node (magnetic field node) on the mirror surface [19]. In this case, an additional spacer layer is not necessary, and thus the absorbing material can be placed directly on top of the mirror surface where the electric field is maximized.

To achieve broadband single-channel CPA in the visible or near-infrared (NIR) region, a PMM-like reflector operating in the corresponding wavelength region is required. However, achieving a PMM in the visible to NIR region is much more difficult than one that operates in the gigahertz to terahertz region, because the required structural dimensions decrease proportionally with the operation wavelength. Recently, a PMM operating over the visible region was demonstrated using nano-gratings, but it was difficult to fabricate, resulting in high fabrication cost and large-area incompatibility [19,20]. Moreover, such a PMM is typically designed only for a single input polarization, and its operation is strongly polarization-dependent [19].

In this work, we propose a pseudo PMM (PPMM), a simple planar dielectric layer on top of a metal layer, which shows significantly enhanced incident angle range and insensitivity to the input polarization state over a broad wavelength range in the visible or NIR region. Since it does not require complex patterning processes, PPMM can also be fabricated over the large area. By combining the PPMM with an ultrathin high-index absorbing material, we theoretically and experimentally demonstrate broadband single-channel CPA in the visible or NIR (900~1600 nm) region.

2. Result and discussion

2.1. Two-channel and single-channel CPA

A schematic illustration of the two-channel CPA is provided in Fig. 1(a). An absorber with a refractive index of $\tilde{n}$ ($= n + i\kappa$) is placed at the center, where the incident medium's refractive index is n_0. In our case, the absorber material was set to platinum (Pt) and n_0 to air ($n_0 = 1$). Two coherent sources with the same intensity counter propagate toward the absorbing material (thickness of $2d$) with a relative phase difference of ϕ. Due to the symmetry, the total reflection (transmission) coefficients from the sources A and B, namely r_A and r_B (t_A and t_B), should be identical to each other. The reflection (r_A, r_B) and transmission (t_A, t_B) coefficients are given by

$$r_A = r_B = r + tt'r'e^{i4\tilde{n}kd}(1 + r'r'e^{i4\tilde{n}kd} + \cdots) = r + \frac{(1 - r^2)r'e^{i4\tilde{n}kd}}{1 - r^2e^{i4\tilde{n}kd}} \quad (1)$$

$$t_A = t_B = tt'e^{i2\tilde{n}kd}(1 + r'r'e^{i4\tilde{n}kd} + \cdots) = r + \frac{(1 - r^2)r'e^{i2\tilde{n}kd}}{1 - r^2e^{i4\tilde{n}kd}}, \quad (2)$$

where k is a wavenumber ($k = 2\pi/\lambda$), and r and t are the Fresnel reflection and transmission coefficient at the interface ($r = (n_0 - \tilde{n})/(n_0 + \tilde{n})$, $r' = -r$, $t = 1 + r$, $t' = 1 - r$), respectively. CPA is achieved when $r_A + t_B = 0$ for symmetric coherent illuminations ($\phi = 0, 2\pi, 4\pi\ldots$) or $r_A - t_B = 0$ for anti-symmetric coherent illuminations ($\phi = \pi, 3\pi, 5\pi\ldots$) [10]. The conditions for both cases can be expressed as

$$e^{i2\tilde{n}kd} = \pm\frac{\tilde{n} - n_0}{\tilde{n} + n_0}. \quad (3)$$

For example, when the operation wavelength λ is 1200 nm in Eq. (3), the corresponding Pt thickness $2d$ for the CPA is around 9.0 nm ($kd << 1$). The output intensity versus the relative phase difference (ϕ) between the two coherent sources for this case is shown in the bottom panel of Fig. 1(a). The CPA occurs around (but not exactly at) the in-phase condition ($\phi \sim 0, 2\pi, 4\pi\ldots$) for the symmetric illumination case, and the out-of-phase condition ($\phi \sim \pi, 3\pi, 5\pi\ldots$) for the anti-symmetric illumination case.

Interestingly, single-channel CPA with an ideal reflector (PMM or PEM) can also create a situation that is identical to that of the two-channel CPA. When we place a PMM or PEM at the

Optics EXPRESS

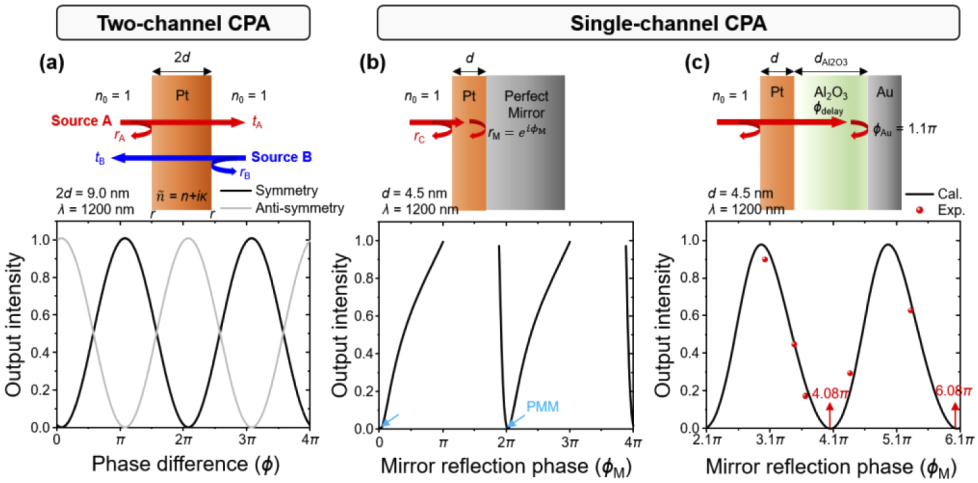

Fig. 1. Basic concept of two-channel and single-channel CPA. (a) Schematic illustration of two-channel CPA is shown in the top panel. The optical absorber (Pt in our case) is placed at the center and the refractive index of the incident medium (n_0) is 1. The graph of the output intensity versus phase difference (ϕ) for the absorber thickness of $2d = 9.0$ nm at $\lambda = 1200$ nm is shown in the bottom panel. Symmetrical (anti-symmetrical) illuminations exhibit the CPA around the in-phase (out-of-phase) condition. (b) Schematic illustration of single-channel CPA with the Pt absorber on a perfect mirror. The perfect mirror reflects 100% of the incident light and the reflection phase (ϕ_M) varies from 0 to 4π. The CPA occurs when ϕ_M is around the in-phase condition (symmetrical case). (c) Experimental demonstration of the single-channel CPA with the optically thin Pt absorber on a phase-controlled mirror (Al_2O_3/Au). The x-axis of the graph represents the total reflection phase, which is composed of the phase delay in the Al_2O_3 layer ($2kn_{Al2O3}d_{Al2O3}$) and the reflection phase at the Al_2O_3/Au interface (ϕ_{Au}). The calculated output intensity (black line) is almost the same with the symmetrical case in Fig. 1(a). The red circle scatters represent experimentally measured output intensities.

center of the absorber (thickness of d; note that it is half of the two-channel case) as shown in Fig. 1(b), the reflection coefficient can be expressed as

$$r_C = r + tt' r_M e^{i2\tilde{n}kd}(1 + r_M r' e^{i2\tilde{n}kd} + \cdots) = r + \frac{(1 - r^2) r_M e^{i2\tilde{n}kd}}{1 - r r_M e^{i2\tilde{n}kd}} \tag{4}$$

where r and r_M are the reflection coefficient at the air/Pt and perfect mirror interface, respectively. We can set r_M to either +1 or –1 for PMM and PEM, respectively, because the reflection phase at the PMM (or PEM) interface is 2π (or π). Assuming that no light is transmitted through the perfect mirror, the condition for no reflection ($r_C = 0$) is completely equivalent to Eq. (3). As a result of this, the PMM and PEM cases correspond to the symmetric and anti-symmetric illumination, respectively. When the absorbing material is not optically thin, the solutions for Eq. (3) becomes discrete and inevitably results in narrowband CPA, whereas the optically thin absorbing film ($kd << 1$) allows broadband solutions [15]. However, an optically thin absorber on a PEM provides no solution for normal incidence. Therefore, single-channel broadband CPA using an ultrathin absorber can only be achieved with a PMM. For example, when the ideal perfect mirror, whose reflectance is always 1 and the reflection phase (ϕ_M) varies from 0 to 4π, is placed under a 4.5 nm-thick Pt absorber [Fig. 1(b), (d) = 4.5 nm], CPA (no reflection) can be observed around the in-phase condition ($\phi = 0.02\pi, 2.02\pi, 4.02\pi$), which corresponds to the PMM. For experimental verification, we placed an optically thin absorber (4.5 nm-thick Pt

Optics EXPRESS

layer) on top of a metallic mirror with a controlled phase delay (a dielectric Al_2O_3 layer on an optically thick gold (Au) layer), as shown in Fig. 1(c). Total reflection phase of the mirror (ϕ_M) is composed of the phase delay in the Al_2O_3 dielectric layer (ϕ_{delay}) and the reflection phase at the Al_2O_3/Au interface (ϕ_{Au}). The former, ϕ_{delay}, is determined by the dielectric thickness (d_{Al2O3}), and corresponds to $\phi_{delay} = 2kn_{Al2O3}d_{Al2O3}$ ($n_{Al2O3} = 1.663$ and $\lambda = 1200$ nm). The reflection phase ϕ_{Au} is 1.1π, which is not exactly equal to π because the metal layer (Au) is not perfectly conducting at the operation wavelength. In the bottom graph of Fig. 1(c), the theoretically calculated output intensity versus the total reflection phase ($\phi_M = \phi_{delay} + \phi_{Au}$) is shown (black line), and it is almost identical to the symmetrical illumination (thus PMM) case described in Fig. 1(a). We fabricated five samples with different Al_2O_3 thicknesses, and the experimentally measured output intensities are indicated in the red circle scatters in Fig. 1(c). The experimental results at $\lambda = 1200$ nm agree well with the calculated results, verifying our theory.

2.2. Broadband PPMM with a high-index material

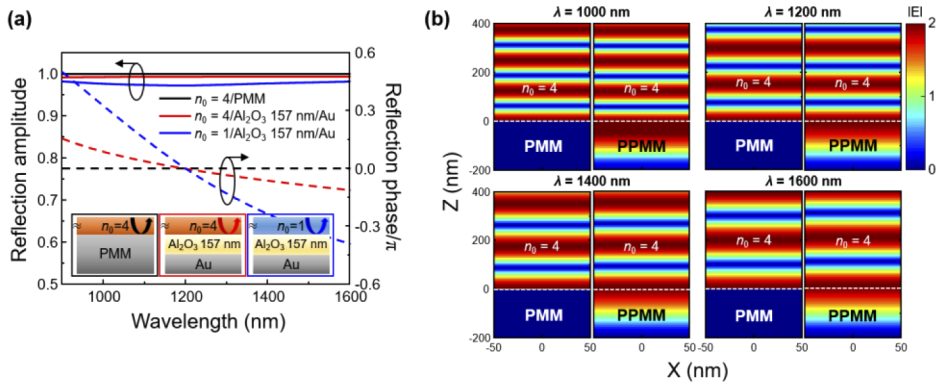

Fig. 2. Characteristics of the broadband PPMM. (a) Total reflection amplitude (solid lines) and phase (dashed lines) at the PMM and PPMM surface under $n_0 = 4$ and 1. The inset shows schematic illustration of the situations. The reflection phase of the PMM is always 0 (or 2π) independent of n_0. The Al_2O_3/Au mirror under $n_0 = 4$ (red lines) shows incident wavelength-insensitive characteristics, resulting in the broadband PPMM, whereas the Al_2O_3/Au mirror under $n_0 = 1$ is a narrow band PMM around 1200 nm. (b) Electric field profiles of the PMM and PPMM under $n_0 = 4$ for the wavelengths of 1000, 1200, 1400, and 1600 nm. The PPMM acts as a broadband PMM.

For broadband single-channel CPA, a PMM should also operate over a broad range of input wavelengths. The PMM completely blocks an incident magnetic field and thus the reflection phase of the magnetic field is π, while the reflection phase of an incident electric field is 0. As a result, at the PMM surface, the magnetic field is zero (node) and the electric field is maximized by constructive interference between the incident and reflected waves (anti-node). In Fig. 2(a), we present the (electric field's) reflection amplitude and the phase of the ideal PMM using solid and dashed black lines, respectively. They are always 1 and 0, respectively, independent of the incident wavelength (λ) and the incident medium's refractive index (n_0). In Fig. 2(b), the electric field profiles with a PMM under the incident medium of $n_0 = 4$ show that the electric field is indeed maximized at the PMM surface (white dashed line) regardless of the input wavelength ($\lambda = 1000$, 1200, 1400, and 1600 nm).

Our proposed broadband PPMM is composed of a simple planar 157 nm-thick Al_2O_3 layer (a dielectric phase delay layer) on an optically thick Au layer. A center wavelength (zero total reflection phase, $\phi_M = 0$) was set to around 1200 nm as shown in Fig. 2(a). In general, the mirror properties of the dielectric on metal structure significantly depends on the incident wavelength,

Optics EXPRESS

because the phase delay within dielectric layer strongly depends on the incident wavelength, usually resulting in a narrowband PMM. For example, as shown in Fig. 2(a), the PPMM placed in air ($n_0 = 1$) behaves as a PMM only around 1200 nm (blue dashed line). However, when the PPMM is placed under a high-index medium (*e.g.*, $n_0 = 4$), it almost acts as a PMM over a wider NIR wavelength range (900~1600 nm) and is relatively insensitive to the incident wavelength (red lines). In Fig. 2(b), the electric field profiles for an PPMM under a high-index medium ($n_0 = 4$) prove that our PPMM can indeed emulate the broadband PMM.

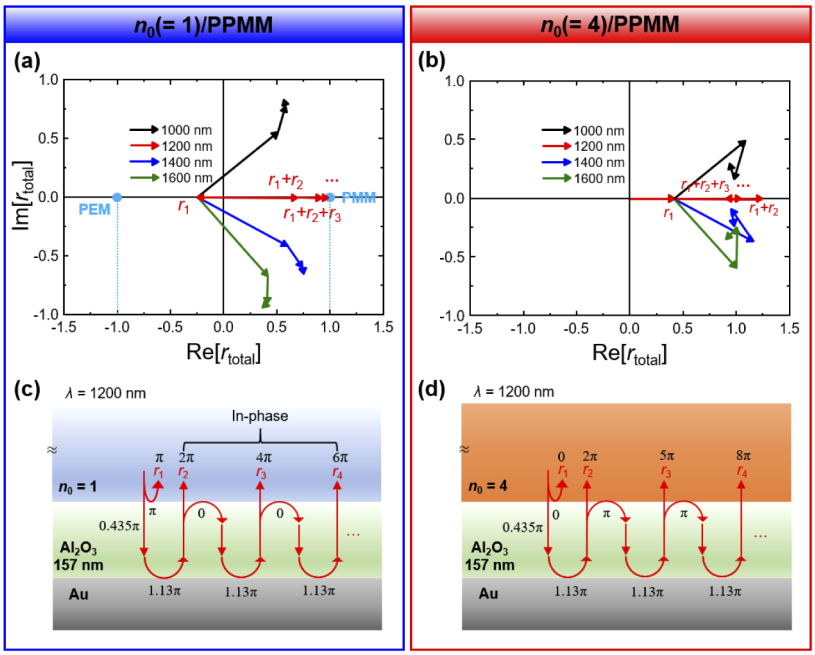

Fig. 3. Interference analysis of the broadband PPMM. The complex amplitude trajectories of the first four partially reflected waves from the PPMM (Al_2O_3 157 nm/Au) under the incident medium with (a) $n_0 = 1$ and (b) $n_0 = 4$, respectively, from Eq. (5). The PPMM under the lower index material ($n_0 = 1$) strongly depends on the wavelength, while the higher index ($n_0 = 4$) material case is relatively insensitive to the input wavelength. Partially reflected waves from the PPMM are illustrated for (c) the lower index and (d) the higher index case ($\lambda = 1200$ nm).

To understand the broadband operation of the PPMM under high-index environments, we illustrate the trajectory of the partially reflected waves for the two cases ($n_0 = 1$ and $n_0 = 4$). The total reflection coefficient can be calculated as

$$r_{\text{total}} = \sum_{q=1}^{\infty} r_q = r_1 + r_1 + t_1' t_1 \sum_{q=2}^{\infty} (r'_1)^{q-2} r_a{}^{q-1} e^{i2(q-1)n_{\text{Al2O3}}kd} \tag{5}$$

where r_q is the q^{th} partially reflected wave, $r_1 = (n_0 - n_{\text{Al2O3}})/(n_0 + n_{\text{Al2O3}})$, $r_a = (n_{\text{Al2O3}} - n_{\text{Au}})/(n_{\text{Al2O3}} + n_{\text{Au}})$, $r_1' = -r_1$, $t_1 = 1 + r_1$, $t_1' = 1 + r_1'$, and $d = 157$ nm. In Figs. 3(a) and 3(b), we show the trajectories of r_{total} in the complex plane obtained by Eq. (5). For the $n_0 = 1$ case, the PPMM acts as the PMM only at the target wavelength of 1200 nm (red arrows), and its reflection phase rapidly varies as the wavelength deviates away from the target wavelength. The reason for this can be visually understood from Fig. 3(c). At 1200 nm, all of the partially reflected waves, r_q ($q > 1$), remain in-phase. Thus, once the input wavelength moves away from the design wavelength of 1200 nm, the partially reflected waves do not collectively contribute to the total reflection phase toward the PMM situation. However, for the $n_0 = 4$ case [Fig. 3(b)], the

Optics EXPRESS

PPMM maintains the PMM characteristics even though the wavelength is far from the design wavelength. As shown in Fig. 3(d), the partially reflected waves still remain out of phase (a phase difference of 3π) due to the reflection phase of π from the Al_2O_3 ($n_{Al2O3} = 1.663$) to $n_0 = 4$, even if the input wavelength is different from the design wavelength (1200 nm).

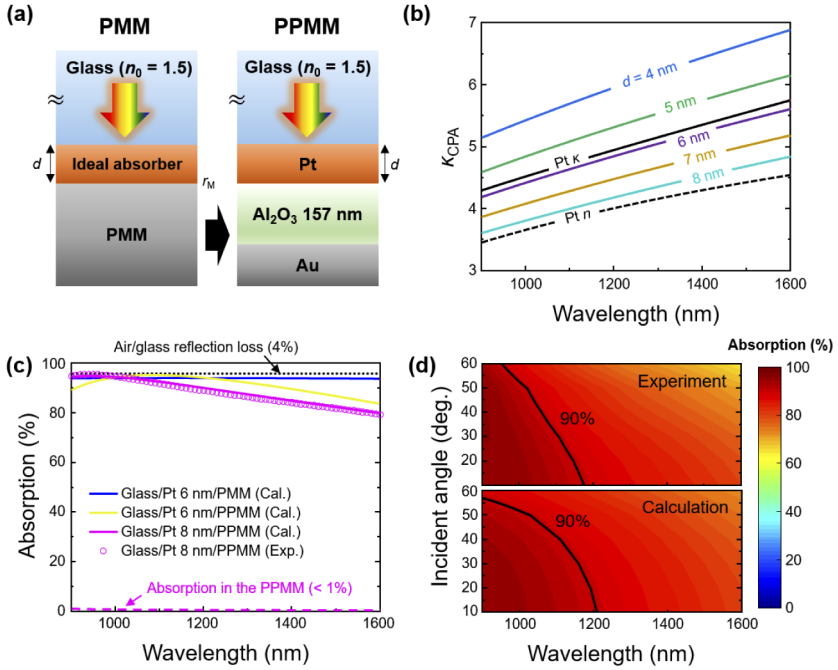

Fig. 4. Broadband single-channel CPA with the PPMM. (a) Schematic structures of the single-channel CPA with the ideal PMM and PPMM (Al_2O_3 157 nm/Au). A glass substrate was used and Pt (thickness of d) was used as the absorber material. (b) κ_{CPA} for different Pt thicknesses ($d = 4\sim8$ nm). κ_{CPA} for the 6 nm-thick Pt case (purple line) nearly corresponds to the actual κ of Pt, indicating that 6 nm-thick Pt can perform as the ideal absorbing material for CPA. (c) Absorption spectra of the 6 nm-thick Pt on the PMM (blue) and PPMM (yellow), and they show almost perfect absorption. The dotted black line represents the maximum absorption limit considering the air/glass Fresnel reflection (4%). The magenta solid line and open circles represent the calculated and experimental results for the 8 nm-thick Pt/PPMM. The absorption by the PPMM is lower than 1%, indicating that most absorption occurs at the Pt absorber. (d) Angle-resolved polarization-averaged absorption from 10 to 60 degrees for the 8 nm-thick Pt/PPMM sample.

2.3. *Broadband single-channel CPA with the PPMM*

In the previous sections, we have derived the condition for broadband single-channel CPA and PPMM. By combining these results, we can design broadband CPA [Fig. 4(a)]. According to Eq. (3), when the parameter values for k, d, n_0 and n (the real part of $\tilde{n}$) are given, we can obtain κ_{CPA} (the imaginary part of $\tilde{n}$), which is the ideal solution for the CPA. Since we cannot arbitrarily change the imaginary part of absorbing material (κ), we instead choose the absorber thickness parameter d, such that κ_{CPA} best matches with the actual κ over the wide wavelength range [Fig. 4(b)]. This method is proven to be very effective when selecting an absorbing material and its thickness [21]. In Fig. 4(b), we calculated κ_{CPA} of an ideal absorber at various absorber thicknesses ($d = 4\sim8$ nm). We set the incident medium to glass ($n_0 = 1.5$) just because we used a glass substrate in our experiments. We used platinum (Pt) as an absorber material because of

Optics EXPRESS

its high refractive index for the broadband PPMM operation. We set n to the real part of the refractive index of a 6 nm-thick Pt layer [dashed black line in Fig. 4(b)], n_0 to 1.5, and d to 4~8 nm. When d is around 6 nm, κ_{CPA} almost matches with the actual extinction coefficient κ of Pt. This means that the 6 nm-thick Pt layer on the PMM almost satisfies the CPA condition. To verify this, we first calculated the absorption of the glass/Pt 6 nm/PMM (blue line) in Fig. 4(c), and the average absorption was higher than 93% (it would have been higher than 97% if there was no reflection loss between the air and glass). Actually, κ_{CPA} obtained from Eq. (3) is complex values, but we only took its real part because the imaginary part is much smaller than the real part, and thus it did not significantly affect the overall reflection. Additionally, the effects of the thickness variation for the Pt and Al_2O_3 layer on the overall CPA absorption are shown in Fig. S1 of the supplemental document. Our systematic approach clearly shows that there exist an optimal range of absorbing layer thicknesses for broadband single-channel CPA operation.

To experimentally realize the broadband single-channel CPA, we placed a Pt absorber on the PPMM (Al_2O_3 157 nm/Au) and measured the wavelength-dependent absorption. It almost perfectly absorbed the incident light around 1100 nm [yellow line in Fig. 4(c)]. The sample structure we fabricated has an 8 nm-thick (instead of 6 nm) Pt layer deposited on the PPMM, since controlling the thickness within a few nanometers is difficult to achieve with our deposition equipment. The experimentally measured (magenta open circles) and calculated (magenta line) absorption of the fabricated sample with an 8 nm-thick Pt layer were in good agreement. The absorption by the PPMM, more specifically by the Au layer in the PPMM, is shown with the magenta dashed line (< 1%), and negligible compared to the absorption in the Pt layer. In addition, we also show the incident angle-resolved absorption (both calculated and measured) of the fabricated sample in Fig. 4(d). The calculated and measured absorption were obtained by averaging s-polarized and p-polarized light. More than 90% absorption was maintained up to the incident angle of 60 degrees around the wavelength of 900 nm. We would like to note that this wide acceptance angle is mainly from the large index contrast between the air and Pt [21]. Moreover, our absorber is also operable in the visible range when a proper PPMM design is employed (See Fig. S2 in the supplement document for such a PPMM design).

The configuration of our absorber appears to be similar to the Salisbury screen. However, Salisbury screen is often applied in the gigahertz to terahertz frequency range [17], and typically operates only within a narrow range of input wavelengths and incident angles. On the other hand, our PPMM with a high-index material might provide much broader operation wavelength range as well as incident angle and polarization insensitivity, which have been often overlooked by the conventional Salisbury screen design.

Our method is not only limited to a specific absorbing material, but can be applied to various other materials. We chose chromium (Cr), titanium (Ti), and tungsten (W) as the absorber candidates. The ideal solutions (κ_{CPA}) for these candidates were calculated using Eq. (3), from the visible to NIR (400~1600 nm), and the results are shown in Figs. 5(a)–5(c). The calculations were conducted using the same method as in Fig. 4(b). The thicknesses of each metal were chosen, such that the ideal κ_{CPA} becomes similar to the actual κ values (black solid line). To verify our methodology, the absorption spectra of each metal on the PMM (solid red line) are shown in Figs. 5(d)–5(f), which confirms high absorption over a wide wavelength region (400~1600 nm) even though the absorption layer thicknesses are thinner than 10 nm. We also show the absorption spectra when the metals are on the PPMM (dotted red lines) in Figs. 5(d)–5(f). The metal/PPMM cases still show high absorption values in the NIR range (900~1600 nm), but exhibit a significant dip near 650 nm. This discrepancy is mainly because the target operation wavelength range of our PPMM design is in the NIR. As we explained above, since only the real parts of κ_{CPA} were considered, the absorption may not reach 100% even if $\mathrm{Re}(\kappa_{CPA})$ is perfectly matched with the actual κ. However, this has no significant impact on the overall broadband CPA operation due to the smaller $\mathrm{Im}(\kappa_{CPA})$ values. We also would like to note that

Optics EXPRESS

this discrepancy in maximum absorption becomes worse for lower n (real part of $\tilde{n}$), which means that the unaccounted $\mathrm{Im}(\kappa_{CPA})$ increases as the real n decreases. Accordingly, noble metals with lower n, such as silver, aluminum, and gold, are not suitable for broadband single-channel CPA operation for the wavelengths longer than the visible region.

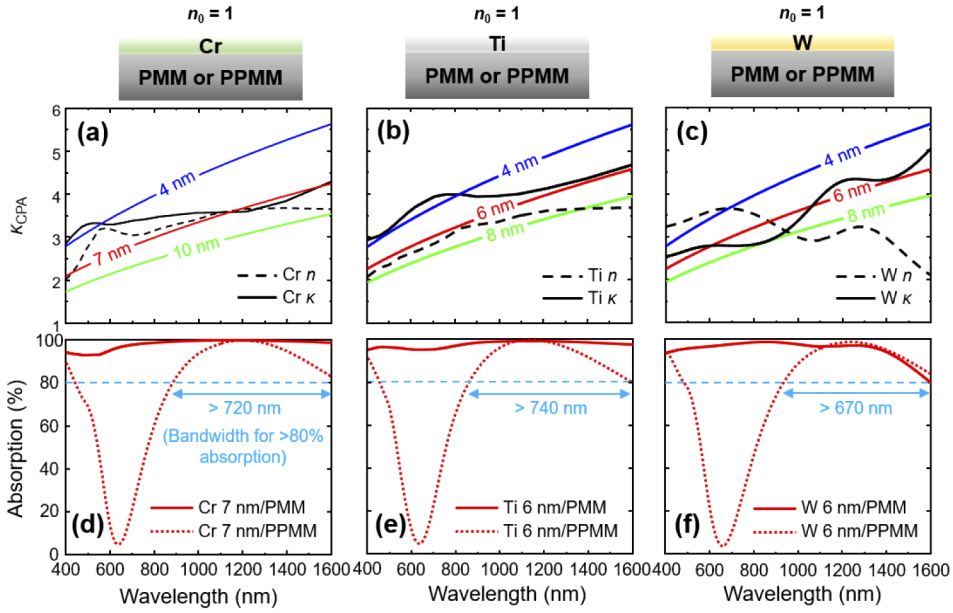

Fig. 5. Single-channel CPA with various metals. Black dashed and solid lines represent n and κ of (a) Cr, (b) Ti, and (c) W. Calculated absorption spectrum for (d) 7 nm Cr, (e) 6 nm Ti, and (f) 6 nm W on the PMM (solid red line) and PPMM (dotted red line). The Al_2O_3 thicknesses of the PPMMs are 157 nm for Cr and Ti, and 170 nm for W, respectively.

3. Experiments and simulations

3.1. Optical simulations and measurements

A transfer matrix method [22] was used to calculate the optical absorption in Fig. 4. The finite differential time domain (FDTD solutions, Lumerical) was used to obtain electric field profiles in Fig. 2(b). Angle-resolved absorption spectra in Fig. 4(d) were calculated by averaging both s-polarization and p-polarization (unpolarized light). Refractive indices of Al_2O_3, Ag, Cr, Ti, and W were obtained from literatures [23–26], except that of Pt from ellipsometry measurements. Absorption spectra in Figs. 4(c) and 4(d) were measured by a UV-visible spectrometer (Lambda 1050, Perkin Elmer). Due to the equipment limitation, the reflection (or absorption) values in Fig. 1(c) and Fig. 4(c) were measured with the incident angle of 10 degrees instead of normal incidence (0 degree incident angle).

3.2. Fabrication

The Pt, Al_2O_3 and Au layer for the samples in Fig. 1(c) and Fig. 4(c) were deposited on a glass substrate by an electron-beam evaporator with a base pressure of 10^{-6} Torr. In Fig. 1(c), the deposition order of the three materials on a glass substrate was Au, Al_2O_3, and Pt. For Fig. 4(c), the deposition order was completely opposite of Fig. 1(c) to make the incident medium's index (n_0) of 1.5. The thickness of the Au layers is 100 nm, which is much thicker than the typical skin depth in the NIR region.

Optics EXPRESS

4. Conclusion

We theoretically and experimentally demonstrated broadband single-channel CPA. We proved that an ultrathin absorbing layer on a PMM can emulate conventional two-channel CPA over a wide range of wavelengths. However, since PMMs are not readily available in nature, we proposed a PPMM scheme capable of operating over a wide range of wavelengths by using a simple planar dielectric layer on a metal layer. Contrary to the prevalent view that the total reflection phase from such a simple structure would be strongly dependent on the incident wavelength, we found that when the PPMM is placed under a high-index material, its reflection phase varies little over a broad wavelength range. Accordingly, by using a high-index material as an absorbing material, we were able to realize broadband single-channel CPA operation across the visible and NIR region. Our patternless PPMM-based single-channel CPA operates over a wide range of incident angles (up to 60 degrees for 93% absorption) regardless of the input polarization state, and can also be easily extended to large area. We expect that our broadband single-channel CPA can be used in versatile applications, such as solar energy harvesting and thermophotovoltaic energy conversion.

Funding

National Research Foundation of Korea (NRF-2016M3D1A1900035).

Disclosures

The authors declare no conflicts of interest.

See Supplement 1 for supporting content.

References

1. Z. Sun, A. Martinez, and F. Wang, "Optical modulators with 2D layered materials," Nat. Photonics **10**(4), 227–238 (2016).
2. M. A. Kats, R. Blanchard, P. Genevet, and F. Capasso, "Nanometre optical coatings based on strong interference effects in highly absorbing media," Nat. Mater. **12**(1), 20–24 (2013).
3. M. L. Brongersma, Y. Cui, and S. Fan, "Light management for photovoltaics using high-index nanostructures," Nat. Mater. **13**(5), 451–460 (2014).
4. W. Li and J. Valentine, "Metamaterial perfect absorber based hot electron photodetection," Nano Lett. **14**(6), 3510–3514 (2014).
5. A. V. Kildishev, A. Boltasseva, and V. M. Shalaev, "Planar photonics with metasurfaces," Science **339**(6125), 1232009 (2013).
6. H.-T. Chen, A. J. Taylor, and N. Yu, "A review of metasurfaces: physics and applications," Rep. Prog. Phys. **79**(7), 076401 (2016).
7. Y. Yao, R. Shankar, M. A. Kats, Y. Song, J. Kong, M. Loncar, and F. Capasso, "Electrically tunable metasurface perfect absorbers for ultrathin mid-infrared optical modulators," Nano Lett. **14**(11), 6526–6532 (2014).
8. J. Park, J.-H. Kang, X. Liu, and M. L. Brongersma, "Electrically tunable epsilon-near-zero (ENZ) metafilm absorbers," Sci. Rep. **5**(1), 15754 (2015).
9. J. Baek, J.-B. You, and K. Yu, "Free-carrier electro-refraction modulation based on a silicon slot waveguide with ITO," Opt. Express **23**(12), 15863–15876 (2015).
10. Y. Chong, L. Ge, H. Cao, and A. D. Stone, "Coherent perfect absorbers: time-reversed lasers," Phys. Rev. Lett. **105**(5), 053901 (2010).
11. W. Wan, Y. Chong, L. Ge, H. Noh, A. D. Stone, and H. Cao, "Time-reversed lasing and interferometric control of absorption," Science **331**(6019), 889–892 (2011).
12. J. Zhang, K. F. MacDonald, and N. I. Zheludev, "Controlling light-with-light without nonlinearity," Light: Sci. Appl. **1**(7), e18 (2012).
13. G. Pirruccio, L. Martin Moreno, G. Lozano, and J. Gómez Rivas, "Coherent and broadband enhanced optical absorption in graphene," ACS Nano **7**(6), 4810–4817 (2013).
14. F. Xiong, J. Zhou, W. Xu, Z. Zhu, X. Yuan, J. Zhang, and S. Qin, "Visible to near-infrared coherent perfect absorption in monolayer graphene," J. Opt. **20**(9), 095401 (2018).

Optics EXPRESS

15. M. Pu, Q. Feng, M. Wang, C. Hu, C. Huang, X. Ma, Z. Zhao, C. Wang, and X. Luo, "Ultrathin broadband nearly perfect absorber with symmetrical coherent illumination," Opt. Express **20**(3), 2246–2254 (2012).
16. R.-H. Yan, R. J. Simes, and L. A. Coldren, "Electroabsorptive Fabry-Perot reflection modulators with asymmetric mirrors," IEEE Photonics Technol. Lett. **1**(9), 273–275 (1989).
17. J. M. Woo, M.-S. Kim, H. W. Kim, and J.-H. Jang, "Graphene based salisbury screen for terahertz absorber," Appl. Phys. Lett. **104**(8), 081106 (2014).
18. S. Li, J. Luo, S. Anwar, S. Li, W. Lu, Z. H. Hang, Y. Lai, B. Hou, M. Shen, and C. Wang, "An equivalent realization of coherent perfect absorption under single beam illumination," Sci. Rep. **4**(1), 7369 (2015).
19. M. Esfandyarpour, E. C. Garnett, Y. Cui, M. D. McGehee, and M. L. Brongersma, "Metamaterial mirrors in optoelectronic devices," Nat. Nanotechnol. **9**(7), 542–547 (2014).
20. S. Liu, M. B. Sinclair, T. S. Mahony, Y. C. Jun, S. Campione, J. Ginn, D. A. Bender, J. R. Wendt, J. F. Ihlefeld, and P. G. Clem, "Optical magnetic mirrors without metals," Optica **1**(4), 250–256 (2014).
21. Y. Jin, J. Park, Y. Rah, J. Shim, and K. Yu, "Ultrahigh omnidirectional, broadband, and polarization-independent optical absorption over the visible wavelengths by effective dispersion engineering," Sci. Rep. **9**(1), 1–10 (2019).
22. L. A. Pettersson, L. S. Roman, and O. Inganäs, "Modeling photocurrent action spectra of photovoltaic devices based on organic thin films," J. Appl. Phys. **86**(1), 487–496 (1999).
23. P. Johnson and R. Christy, "Optical constants of transition metals: Ti, V, Cr, Mn, Fe, Co, Ni, and Pd," Phys. Rev. B **9**(12), 5056–5070 (1974).
24. A. D. Rakić, A. B. Djurišić, J. M. Elazar, and M. L. Majewski, "Optical properties of metallic films for vertical-cavity optoelectronic devices," Appl. Opt. **37**(22), 5271–5283 (1998).
25. K. M. McPeak, S. V. Jayanti, S. J. Kress, S. Meyer, S. Iotti, A. Rossinelli, and D. J. Norris, "Plasmonic films can easily be better: rules and recipes," ACS Photonics **2**(3), 326–333 (2015).
26. R. Boidin, T. Halenkovič, V. Nazabal, L. Beneš, and P. Němec, "Pulsed laser deposited alumina thin films," Ceram. Int. **42**(1), 1177–1182 (2016).